

Untangling competition between epitaxial strain and growth stress through examination of variations in local oxidation

Maria Yankova

University of Manchester <https://orcid.org/0000-0002-0972-6700>

Alistair Garner

University of Manchester

Felicity Baxter

University of Manchester

Samual Armson

University of Manchester

Christopher Race

University of Manchester

Michael Preuss (✉ michael.preuss@monash.edu)

University of Manchester

Philipp Frankel

University of Manchester

Article

Keywords: oxide formation, corrosion, high-performance alloys

Posted Date: October 6th, 2021

DOI: <https://doi.org/10.21203/rs.3.rs-926825/v1>

License: © ⓘ This work is licensed under a Creative Commons Attribution 4.0 International License.

[Read Full License](#)

1 **Untangling competition between epitaxial strain and growth stress through examination** 2 **of variations in local oxidation**

3 **Authors**

4 Maria S. Yankova^{1*}, Alistair Garner¹, Felicity Baxter¹, Samuel Armson¹, Christopher P.
5 Race¹, Michael Preuss^{1, 2†}, Philipp Frankel¹

7 **Affiliations**

8 ¹Materials Performance Centre, Department of Materials, the University of Manchester,
9 Manchester M13 9PL, UK

10 ²Department of Materials Science & Engineering, Monash University, Clayton, 3800,
11 Victoria, Australia

12 *maria.yankova@manchester.ac.uk

13 †michael.preuss@manchester.ac.uk

14 **Abstract**

15 Understanding oxide formation during corrosion of high-performance alloys in harsh
16 environments is of great fundamental and industrial interest and provides a potential route for
17 reducing the significant annual cost of corrosion globally. However, corrosion mechanisms
18 involve multiple length scales, requiring a multitude of advanced experimental procedures.
19 Here, we use correlated high resolution electron microscopy techniques over a range of
20 length scales, combined with crystallographic modelling to show that there is a clear
21 competition between epitaxial strain and growth stress during oxidation. The degree to which
22 these competing mechanisms operate is shown to depend on the orientation of the substrate
23 grains leading to significant local variations in oxide microstructure and thus protectiveness,
24 even across a single sample. This leads to the possibility of tailoring substrate
25 crystallographic textures in order to promote gradual phase transformation and the
26 development of stress driven, well-oriented protective oxides, and so to improving overall
27 corrosion performance.

29 **Main text**

30 As a result of a spontaneous electrochemical reaction with the environment, most metals
31 corrode by forming a metal oxide film. This oxide film may protect the metal substrate
32 against further oxidation depending on a combination of numerous competing mechanisms
33 that operate at a range of length scales. Corrosion costs have been estimated to be around 3%
34 – 4% of each nation's gross domestic product (GDP) or the equivalent of US\$ 2.5 trillion
35 globally in 2013¹. Hence, there is a great financial incentive to reduce corrosion through
36 better understanding of corrosion mechanisms.

37 The crystallographic orientation of the metal grains is an important factor that affects
38 the corrosion rate in many metals and alloys. Studies of both polycrystalline materials²⁻⁴ and
39 single crystals⁵⁻⁷ have shown that corrosion properties can vary significantly over a few
40 degrees difference in crystallographic orientation. The main effect has been attributed to the
41 metallic dissolution rates, expected to scale directly with the surface energy of the
42 crystallographic planes — close-packed planes have a higher atomic density and binding
43 energy, and thus show superior corrosion resistance. This trend was confirmed in
44 experimental studies in a wide range of metals — body-centred-cubic materials, such as Fe²

45 and Cr⁸; face-centred-cubic materials, such as Ni⁹⁻¹¹, Ni-based alloy 22¹², Cu¹³ and Inconel
46 600¹⁴; and hexagonal-close-packed materials, such as Mg^{4,15}, Zn¹⁶, Ti¹⁷ and Zr^{7,18-20}. In
47 parallel, theoretical calculations using first-principles²¹⁻²³ and empirical-potential²⁴⁻²⁶
48 methods confirmed the above hypothesis by calculating the surface energies and energy
49 barriers for diffusion along the different crystal directions.

50 The orientation of the metal grain may also directly affect various aspects of the oxide
51 microstructure — such as crystallographic orientation, oxide phases, grain size and shape.
52 The first is a result of lattice matching between the metal substrate and the growing oxide —
53 that is a preferential adoption of an orientation relationship, or epitaxial relationship, between
54 two lattices, where interfacial planes share similar atomic spacing²⁷. Epitaxial strains develop,
55 which drive the growth of specific crystallographic texture components in the oxide, thus
56 affecting the lattice and grain boundary resistance to diffusion of corroding species. Cathcart
57 et al.⁹ used X-ray diffraction (XRD) to measure the epitaxial orientation relationships in the
58 Ni-NiO system for various faces of single Ni grains. They found a correlation between the
59 fraction of high-angle grain boundaries in NiO and the protectiveness of the oxide layer, later
60 confirmed by other studies^{10,11,28}. In the dual-phase Zr-2.5%Nb alloys with a well-defined
61 substrate texture, bulk XRD oxide texture measurements established lattice matching
62 between different metal faces and the ZrO₂ film during oxide nucleation, followed by a
63 preferential growth of specific oxide orientations²⁹. In contrast, single-phase Zr alloys with
64 typical ‘split-basal’ texture³⁰ (characterised by a 20° to 40° incline of the c-axis of the hcp-Zr
65 lattice with respect to the surface) did not show strong oxide texture or effects on corrosion
66 kinetics³¹. This lack of effect is an artefact of measuring the macrotexture of the material and,
67 as we will show later, metal-oxide orientation relationships do in fact form in single-phase Zr
68 alloys.

69 Another important factor is the volume change associated with the metal-to-oxide
70 transformation, also referred to as the Pilling-Bedworth ratio³². Protective oxides require a
71 ratio larger than one, i.e. the volume of the elementary cell of a metal oxide is larger than that
72 of the corresponding metal, although Pilling-Bedworth ratios larger than two can also be less
73 protective due to oxide buckling^{32,33}. Example of ratios between 1 and 2 are Cu, Ni, Zn, Ti
74 and Zr. Notably, the Pilling-Bedworth-ratio ‘rule’ only applies to those metal-oxide systems
75 in which the oxygen ion diffuses faster through the oxide than the metal ion, resulting in
76 inwards oxide formation. The Zr-ZrO₂ system is a typical example with a Pilling-Bedworth
77 ratio of 1.56 and inwards corrosion — the metal grows a semi-passivating oxide layer under
78 high planar compressive stress³⁴.

79 Associated with the volume expansion of a protective oxide is the build-up of
80 compressive stresses, which can be in the range of several GPa^{35,36}. These large compressive
81 stresses impact oxide grain growth, and thereby grain nucleation, as the oxide will grow so as
82 to minimise its biaxial or triaxial stress state³⁷⁻³⁹. When we consider the influence of the
83 volume change together with the orientation and the elastic anisotropy of the metal crystal, it
84 is possible for particular oxide orientations, which maximise the accommodation of volume
85 changes normal to the interface, to grow preferentially. Gray et al.¹² found that, under certain
86 environmental conditions, the preferential corrosion order of Ni orientations does not follow
87 the surface energy trend. Instead, faces that are more susceptible to corrosion also formed
88 more protective oxide films. Thus, a competition between the epitaxial strain and the growth
89 stress was identified. Moreover, the growth stresses may stabilise otherwise metastable
90 phases of the oxide, in addition to other stabilising factors such as small grain size and
91 chemical dopants^{34,40}. During the oxidation of zirconium alloys in typical light-water nuclear
92 reactor operating conditions, the metastable hexagonal sub-oxide ZrO⁴¹ as well as metastable
93 tetragonal ZrO₂ along with the stable monoclinic ZrO₂ are often observed^{34,42,43}. The role of

94 these metastable phases in the corrosion process is still unclear — phase transformations have
95 been suggested to cause cracking of the oxide film³⁶.

96 Finding strategies for improved corrosion and oxidation control of engineering alloys
97 exposed to harsh environments is key to improving the lifetime of components and even
98 incremental improvements can have substantial consequences: for example, slight
99 improvements in the corrosion performance of zirconium alloys, used to encapsulate nuclear
100 fuel, can dramatically improve efficiencies of nuclear power generation⁴⁴. To date, our
101 understanding of the interplay between metal-oxide crystallographic orientation relationships
102 and oxide growth stresses (and the effect of this interplay on the protectiveness of the oxide)
103 is very limited due to experimental challenges when analysing highly stressed,
104 nanocrystalline oxides over a sufficiently large area or volume. Although bulk techniques
105 such as XRD provide good statistics, they commonly lack the required resolution to directly
106 relate oxide texture to specific metal grain orientations or can only be used in single crystal
107 examinations^{7,9,11,28,45}. Alternatively, transmission electron microscopy (TEM)
108 investigations^{19,28,46,47} only focus on a few oxide grains formed on a single randomly selected
109 substrate grain, making a statistical analysis of possible orientation relationships very
110 difficult. By definition, these techniques also require the production of electron transparent
111 samples, which is known to alter the microstructure of such stress-stabilised oxide films^{48,49}.

112 In the present study, we exploit recent technological advances in electron microscopy
113 combined with modelling of idealised crystallographic orientation relationships to directly
114 relate the orientation of a large number of oxide grains to that of the underlying metal grains
115 on a bulk sample, thereby maintaining the constraint in the oxide. To achieve this, we used
116 electron backscatter diffraction (EBSD) at low accelerating voltage to reliably analyse the
117 phase and orientation of a region containing approximately half a million ZrO₂ nanograins,
118 followed by analysis of the underlying metal microstructure. We then used scanning
119 precession electron diffraction (SPED) in the TEM to relate the observations to the grain
120 morphology and microtexture of the oxide. In addition, we developed an algorithm to identify
121 an epitaxial orientation relationship between any two crystals, which takes as an input EBSD
122 or SPED orientation data. Through modelling of the possible ideal crystallographic
123 orientation relationships, we have identified new zirconium metal-oxide orientation
124 relationships and the competition between the transformation stress and the epitaxial lattice
125 matching mechanisms during oxide growth affecting both the oxide texture development and
126 oxide phase stabilisation. Our multi-scale analysis approach combined with modelling
127 provides new understanding of the main driving forces for oxide texture and microstructure
128 evolution during aqueous corrosion that is applicable to engineering alloys that display
129 inwards corrosion and have a Pilling-Bedworth ratio between 1 and 2.

130 **Results**

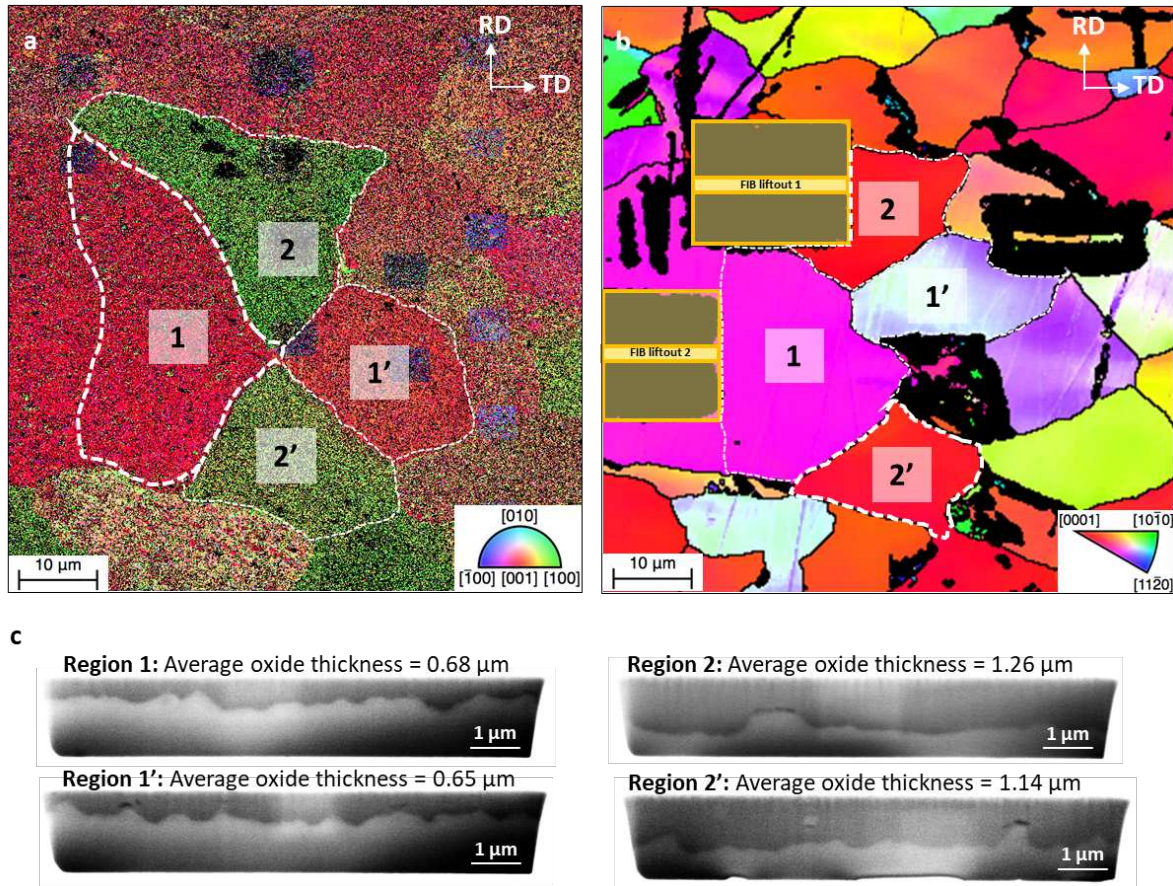
131 *Electron backscatter diffraction*

132 After mechanical removal of the rough outer oxide (removing about 400 nm from an average
133 initial thickness of ~1.2 μm) formed during aqueous corrosion of a commercial single-phase
134 Zr alloy (Zircaloy-2) in a simulated pressurised water reactor (PWR) environment, an EBSD
135 orientation map was acquired from the polished oxide surface, as seen in **Error! Reference**
136 **source not found.**a. The map was obtained using a low accelerating voltage in order to
137 minimise the electron interaction volume and clearly shows that the nanosized oxide grains
138 are grouped into regions with similar crystallographic texture, as outlined and numbered in
139 the figure. Due to the 100-nm step size relative to the average oxide grain diameter of 40–60
140 nm when viewed in this orientation^{39,47}, each data point most likely corresponds to a unique
141 oxide grain. As a result, we obtained a map containing approximately 560,000 oxide grains

142 with 95% of indexed points being stable monoclinic ZrO₂ (m-ZrO₂) and 5% being metastable
143 tetragonal ZrO₂ (t-ZrO₂) (stabilised by a combination of small grain size⁴⁰, stress⁵⁰ and
144 oxygen vacancies⁵¹). Monoclinic ZrO₂ is the stable phase of zirconia at temperatures up to
145 1170°C with four ZrO₂ units per unit cell⁵², whereas between 1170°C and 2370°C the body-
146 centred tetragonal (bct) ZrO₂ phase with two ZrO₂ units per unit cell is stabilised. This crystal
147 structure can also be described by a non-primitive face-centred tetragonal (fct) unit cell
148 containing four ZrO₂ units, and so comparison between orientations is based on bct Miller
149 indices of the tetragonal cell and equivalent fct indices of the monoclinic cell.

150 A grain orientation map acquired from the Zr substrate after mechanical removal of the
151 oxide is shown in **Error! Reference source not found.b**. The stable phase α -Zr has a
152 hexagonal close-packed crystal structure and hereinafter we refer to that phase as simply Zr.
153 Upon comparison with **Error! Reference source not found.a**, there is a strong suggestion
154 that the borders of the microtextured oxide areas are related to the orientation of the
155 underlying metal grains. The regions/grains are highlighted accordingly in **Error! Reference**
156 **source not found.a** and **b**. The lack of a perfect match can be explained by the difficulty in
157 identifying the exact point at which the metal-oxide interface is reached during removal of
158 the oxide film. In **Error! Reference source not found.c** cross-sectional SEM images
159 acquired from FIB trenches from each oxide region show the oxide in regions 2 and 2' to be
160 twice as thick as that in regions 1 and 1'. Further analysis comparing oxide microstructure
161 and crystallographic texture was performed on oxide regions 1 and 2, and the corresponding
162 metal grains. Data from oxide regions 1' and 2' were found to agree with those from regions
163 1 and 2, respectively, and results are included as supplementary material.

164 Firstly, we consider the overall crystallographic texture of the metal grains and oxide
165 regions as measured using EBSD in the contour pole figures in Fig. 2. As seen in **Error!**
166 **Reference source not found.a**, the Zr hcp crystal of grain 1 is positioned so that the basal
167 pole $\langle 0002 \rangle_{\text{Zr}}$ is inclined at about 46° to the normal direction (ND). This inclination is just
168 outside the peak range of 20° to 40° corresponding to the typical crystallographic texture in
169 single-phase Zr alloys used in the nuclear industry^{30,53}. This texture is called 'split-basal' due
170 to a symmetrical 'split' of the hcp basal pole with respect to ND³⁰. In oxide region 1, we
171 measured 49,938 monoclinic grains and 1,847 tetragonal grains, or a tetragonal phase fraction
172 of 3.6%. We observe that the $\langle 001 \rangle$ poles of both the monoclinic and the few indexed
173 tetragonal grains in this region are oriented strongly in the oxide growth direction. The
174 tetragonal $\langle 001 \rangle$ also shows four other peaks positioned at 90° with respect to ND. **Error!**
175 **Reference source not found.2b** shows that the $\langle 0002 \rangle$ pole of the hcp Zr crystal in substrate
176 grain 2 is close to parallel to the normal direction, oriented at 12°. In oxide region 2, the
177 $\langle 001 \rangle$ tetragonal ZrO₂ pole figure is formed from 531 tetragonal grains, which, although a
178 limited number, shows a very close to random crystallographic texture. On the other hand,
179 the $\langle 001 \rangle$ pole figures, formed from 20,544 measured monoclinic oxide grains, exhibit a
180 six-fold symmetry with stronger preference for two of the texture variants. There is a lower
181 tetragonal phase fraction of 2.5% compared with region 1.



182

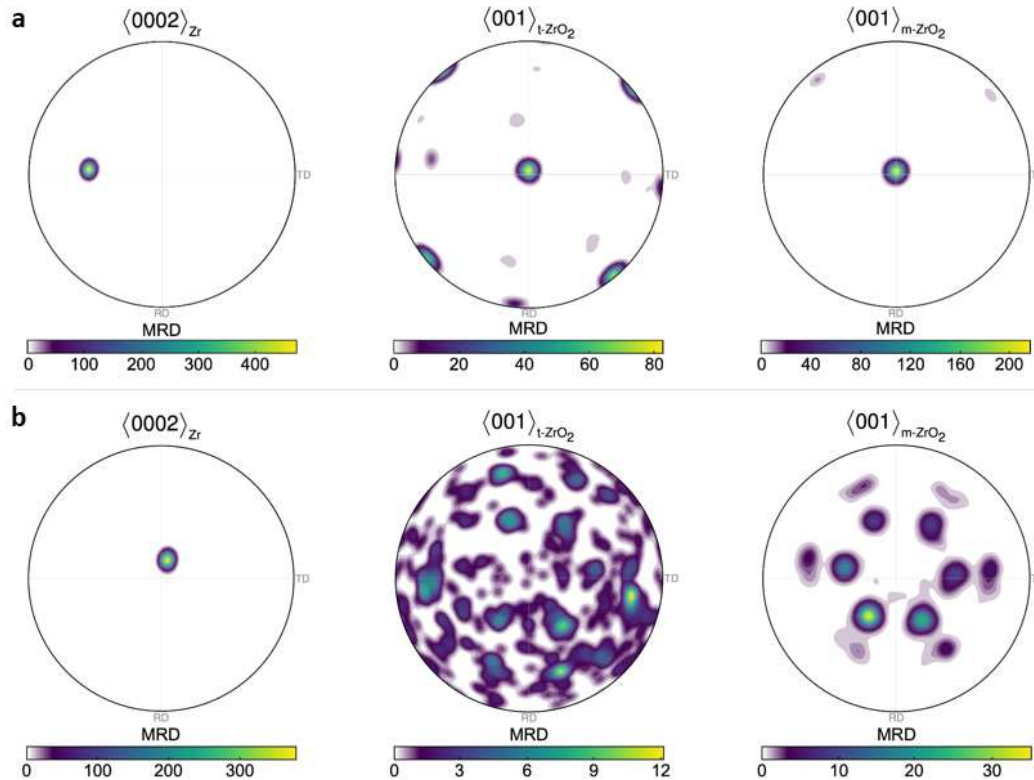
183 **Fig. 1 Electron backscatter diffraction orientation maps.** EBSD orientation maps in
 184 inverse pole figure colouring relative to ND for **a** monoclinic ZrO₂ and **b** corresponding metal
 185 grains after mechanical removal of oxide. Regions for subsequent orientation analysis are
 186 labelled. Original rolling (RD) and transverse (TD) directions are marked on the figures.
 187 SEM images acquired from FIB trenches from each oxide region are shown in **c**. Square
 188 regions (~5 μm) visible in the oxide orientation map are regions of intentional focused-ion-
 189 beam (FIB) damage that formed part of another study⁴⁹ and are excluded from this analysis.
 190

191

192 Plotting the raw pole figures from the EBSD map for the tetragonal and the
 193 monoclinic ZrO₂ phases in region 1, Fig. 3a and c, suggests the presence of lattice matching
 194 between the metal substrate phase and the tetragonal and/or the monoclinic oxides. We
 195 performed further analysis by calculating possible theoretical orientation relationships, which
 196 revealed two scenarios. In the first one, denoted by pink discs in Fig. 3c, hcp Zr transforms to
 197 tetragonal ZrO₂, and then the tetragonal grains transform to monoclinic ZrO₂ based on the
 198 relationships: $\{111\} \langle 10\bar{1} \rangle_{m-ZrO_2} \parallel \{101\} \langle 11\bar{2} \rangle_{t-ZrO_2} \parallel \{0002\} \langle 11\bar{2}0 \rangle_{Zr}$. In the
 199 second one, denoted by blue crosses in Fig. 3c, hcp Zr can still transform to tetragonal ZrO₂
 200 according to $\{101\} \langle 11\bar{2} \rangle_{t-ZrO_2} \parallel \{0002\} \langle 11\bar{2}0 \rangle_{Zr}$, and it can also transform directly
 201 to monoclinic ZrO₂ according to $\{111\} \langle 10\bar{1} \rangle_{m-ZrO_2} \parallel \{0002\} \langle 11\bar{2}0 \rangle_{Zr}$. We observe
 202 almost equal proportion of the four experimentally measured texture components in the
 $\{001\}_{m-ZrO_2}$ and $\{10\bar{1}\}_{m-ZrO_2}$ pole figures, which are matched by the theoretical
 203 orientations of the first scenario. Therefore, we conclude that the majority of the oxide has
 204 formed as a tetragonal phase first, and then transformed to monoclinic. That resolves a long-
 205 standing issue of which ZrO₂ phase forms first and has important implications for the
 206 corrosion process of Zr alloys to be discussed later. It should also be pointed out that during a

207 hexagonal-close-packed to tetragonal phase transformation, 24 possible symmetrically
208 equivalent variants exist. However, the hcp crystal is only 3-fold rotationally symmetric, and
209 so 12 of the symmetry variants might grow on an exposed A layer of the hcp stacking and
210 another 12 might grow on an exposed B layer. We only observed one of these 12-variant sets
211 in the measured tetragonal phase, which we attribute to a random process due to the
212 transformation of a single Zr grain. In the next phase transformation, from tetragonal to
213 monoclinic ZrO_2 , we note that 4 of the 12 variants have grown preferentially, as seen in Fig.
214 2 (C), to form a strong epitaxial texture with the $\{10\bar{6}\}_{m-ZrO_2}$ parallel to the metal-oxide
215 interface. Raw pole figure data plotted from the EBSD maps of the tetragonal and the
216 monoclinic ZrO_2 in region 2 are shown in **Error! Reference source not found.**3b and d.
217 Here, the tetragonal grains do not exhibit a preferential texture. On the other hand, the
218 $\{001\}_{m-ZrO_2}$ pole figure in d clearly shows two distinct texture components. We looked at
219 different possible oxide orientations that could arise from lattice matching between the hcp Zr
220 lattice and the monoclinic ZrO_2 lattice, and in order to reproduce the experimental results the
221 inclusion of two new epitaxial relationships between the monoclinic oxide and the metal
222 substrate was required. We have identified both of these components to have the $\langle 111 \rangle$
223 monoclinic oxide directions parallel to the $\langle 1\bar{1}00 \rangle$ Zr directions but with either the $\{11\bar{2}\}$ or
224 the $\{31\bar{2}\}$ oxide planes parallel to the $\{0002\}$ metal plane. The theoretical orientations based
225 on these two epitaxial relationships, i.e. $\{11\bar{2}\} \langle 111 \rangle_{m-ZrO_2} \parallel \{0002\} \langle 1\bar{1}00 \rangle_{Zr}$ and
226 $\{31\bar{2}\} \langle 111 \rangle_{m-ZrO_2} \parallel \{0002\} \langle 1\bar{1}00 \rangle_{Zr}$, and the assumption of the metal $\langle 0002 \rangle_{Zr}$
227 being normal to the metal-oxide interface, are overlaid as orange disks and red crosses,
228 respectively. We see an excellent match between the model and the experimental textures.
229 The fraction of the major texture component was found to be approximately 2.4 times that of
230 the minor component and both components have a spread of 16° from the ideal orientation
231 for reasons described previously.

232



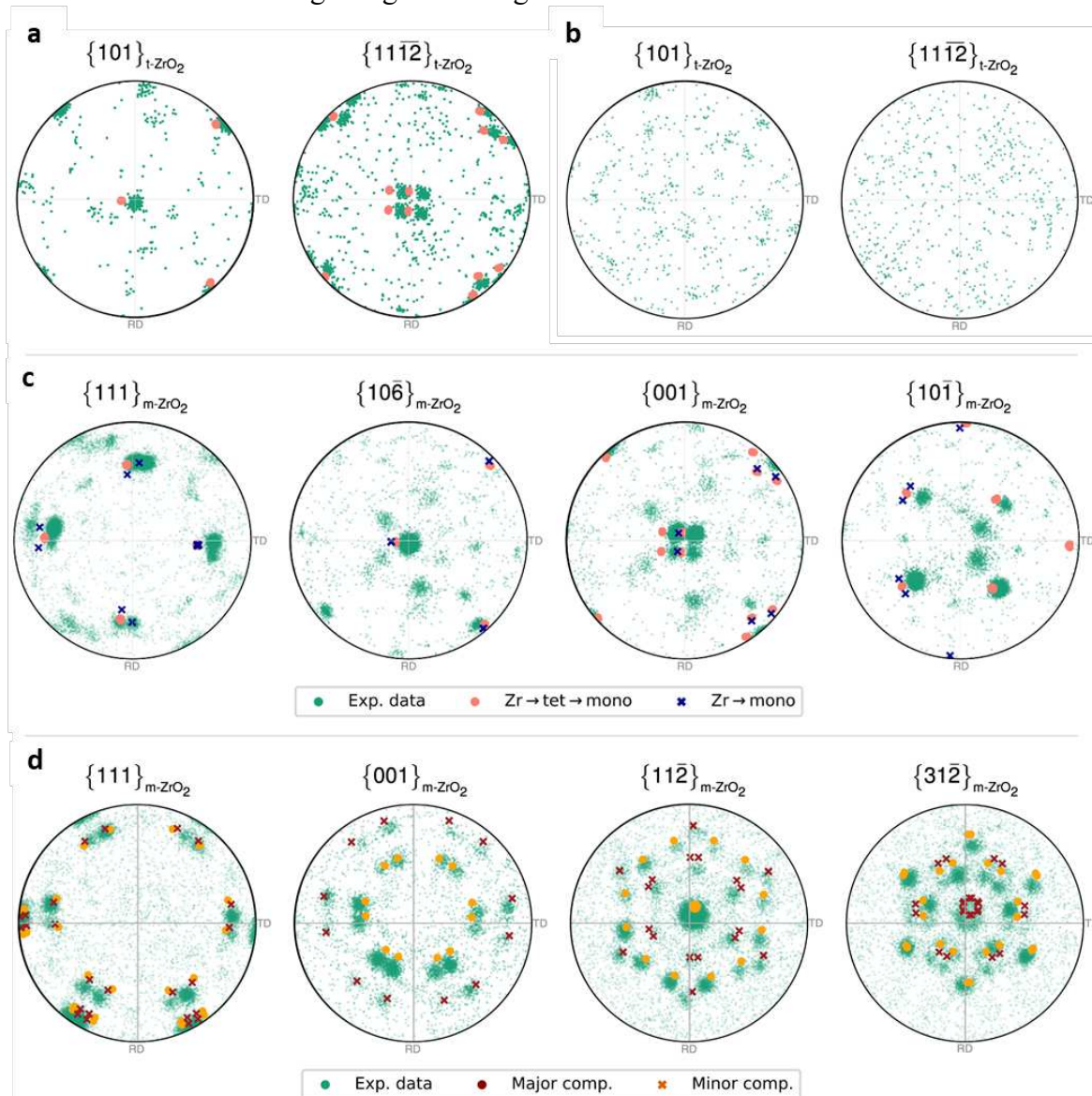
233
234
235
236
237
238
239

Fig. 2 Electron backscatter diffraction contour pole figures. Contoured pole figures for the $\langle 0002 \rangle_{\text{Zr}}$ pole in hexagonal Zr, and the $\langle 001 \rangle$ poles in tetragonal and monoclinic ZrO_2 in metal grain 1 and oxide region 1 (a); metal grain 2 and oxide region 2 (b). All contoured pole figures are normalised to multiples of a random distribution (MRD) and oriented to be consistent with EBSD map in Fig. 1 with TD \parallel x axis, RD \parallel y axis and ND \parallel z axis.

240 *Scanning precession electron diffraction*

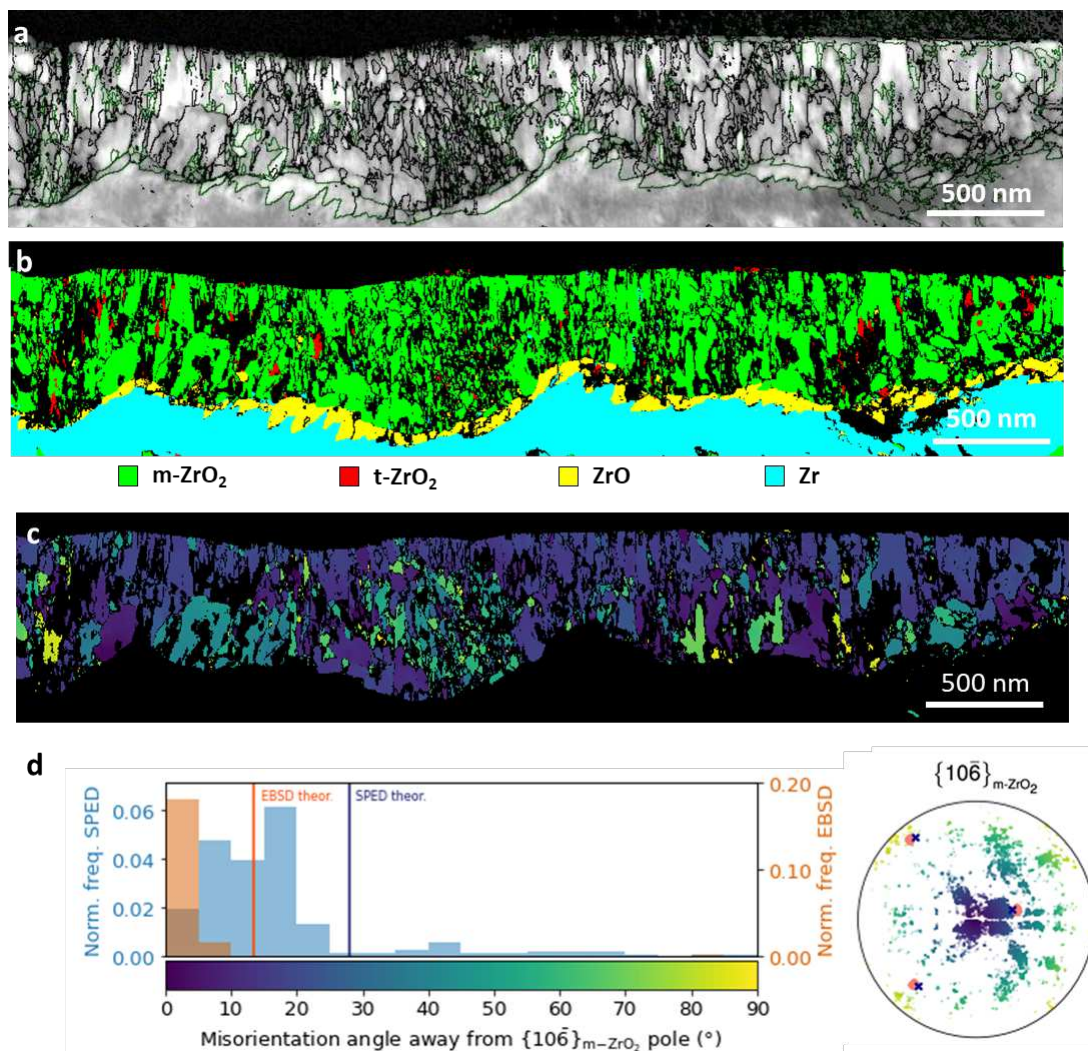
241 A SPED correlation index map for region 1 is shown in **Error! Reference source not**
 242 **found**.a. The correlation index is a measure of the quality of matching between the
 243 experimental and theoretical diffraction patterns from template matching⁵⁴ and can be used
 244 to visualise microstructural features analogous to band contrast maps produced from EBSD
 245 measurements (see experimental methods for more details on the SPED technique). The map
 246 is overlaid with monoclinic grain boundaries defined by a misorientation threshold of 5° to
 247 emphasise the oxide microstructure and to enable grain size analysis. In region 1, the oxide
 248 grains are ordered and exhibit a uniform oxide microstructure with an average grain width of
 249 ~ 57 nm. In Fig. 4b the SPED phase map from region 1 clearly shows that most of the oxide is
 250 composed of monoclinic ZrO_2 with a minor tetragonal phase fraction in this region around
 251 2% and a continuous layer of ZrO sub-oxide. Fig. 4c**Error! Reference source not found**.
 252 shows the SPED orientation map of the monoclinic oxide formed in region 1, which is
 253 coloured according to deviation of the $\{10\bar{6}\}_{\text{m-ZrO}_2}$ pole from the oxide growth direction. As
 254 shown in the frequency distribution in Fig. 4d, the SPED measured texture exhibits a larger
 255 spread compared with the EBSD measured data. The corresponding theoretical variants with
 256 a misorientation angle from the $\{10\bar{6}\}_{\text{m-ZrO}_2}$ pole closest to zero are also plotted. The
 257 theoretical orientations are calculated based on the measured substrate orientation using the
 258 corresponding microscopy technique. The difference between the EBSD and the SPED

259 measurements as well as between the experimental and the theoretically predicted
 260 orientations can be attributed to several factors: misalignment between the samples used in
 261 each technique, internal misorientations within the metal grain, misindexing of some SPED
 262 data and relative surface orientation before/after oxide removal. The SPED $\{10\bar{6}\}_{m-ZrO_2}$ pole
 263 figure in Fig. 4d confirm the monoclinic texture measurement obtained using EBSD and
 264 again are overlaid with the orientations arising from the proposed theoretical orientation
 265 relationships. There is a strong alignment of the $\{10\bar{6}\}_{m-ZrO_2}$ poles in the oxide growth
 266 direction, but with a larger spread from the theoretical orientation relationships due to the
 267 smaller number of investigated grains using SPED.

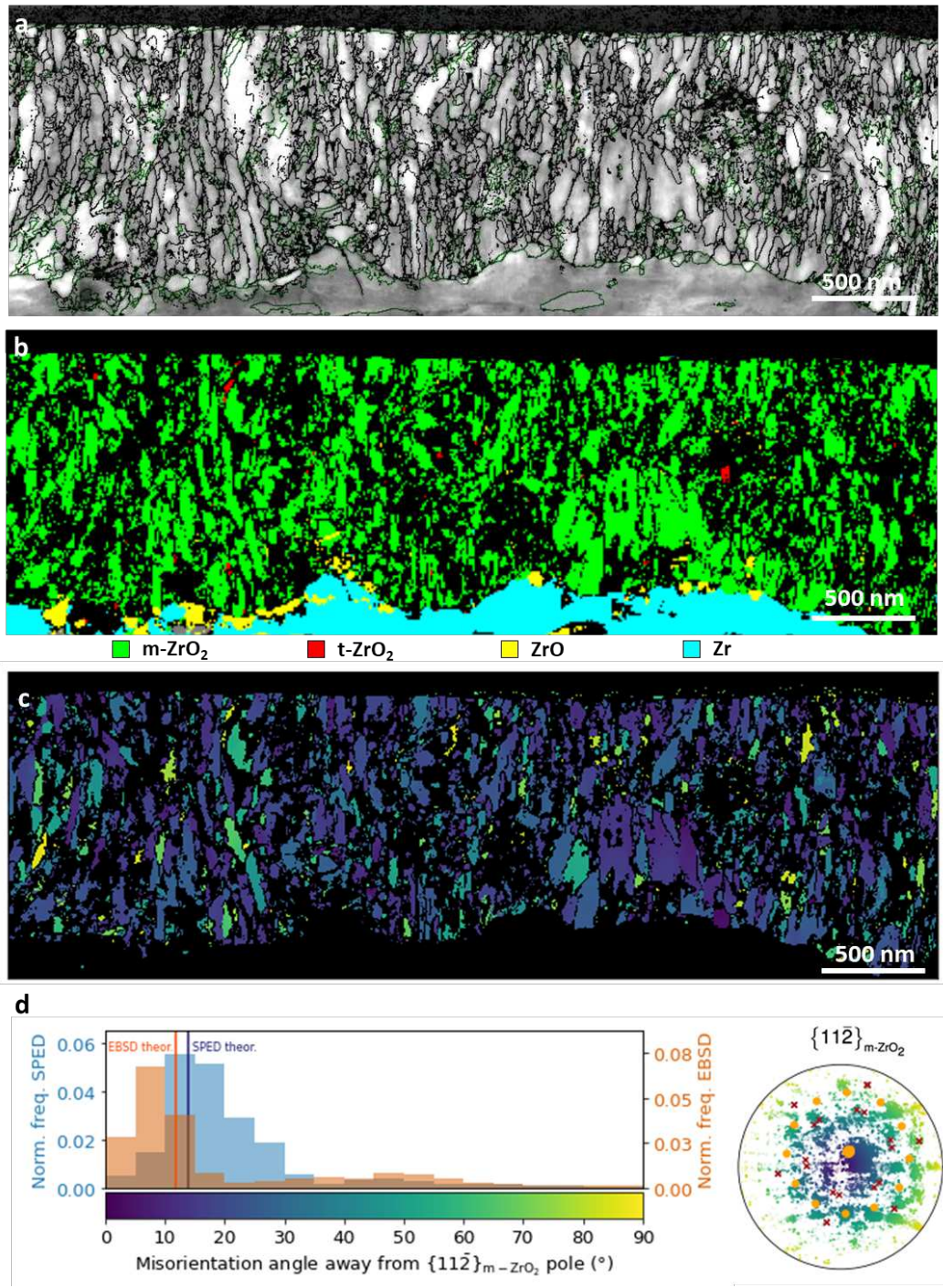


268
 269 **Fig. 3 EBSD and theoretical crystallographic orientation data.** a, b Raw pole figures for
 270 equivalent poles $\{101\}$ and $\{11\bar{1}2\}$ of tetragonal ZrO_2 in oxide region 1 (a) and 2 (b). c Raw
 271 pole figures of monoclinic ZrO_2 for equivalent poles $\{111\}$, $\{10\bar{6}\}$, $\{001\}$ and $\{10\bar{1}\}$ in
 272 oxide region 1. Denoted with pink disks and blue crosses are possible theoretical orientation
 273 relationships $\{111\} \langle 10\bar{1} \rangle_{m-ZrO_2} \parallel \{101\} \langle 11\bar{2} \rangle_{t-ZrO_2} \parallel \{0002\} \langle 11\bar{2}0 \rangle_{Zr}$ and
 274 $\{111\} \langle 10\bar{1} \rangle_{m-ZrO_2} \parallel \{0002\} \langle 11\bar{2}0 \rangle_{Zr}$, respectively. d Raw pole figures for
 275 equivalent poles $\{111\}$, $\{001\}$, $\{11\bar{2}\}$ and $\{31\bar{2}\}$ of monoclinic ZrO_2 in oxide region 2.

276 Denoted with orange disks and red crosses are the major and minor theoretical orientation
 277 relationships $\{112\} \langle 111 \rangle_{m\text{-ZrO}_2} \parallel \{0002\} \langle 1100 \rangle_{\text{Zr}}$ and $\{312\} \langle$
 278 $111 \rangle_{m\text{-ZrO}_2} \parallel \{0002\} \langle 1100 \rangle_{\text{Zr}}$. All contoured pole figured are normalised to multiples
 279 of a random distribution (MRD) and oriented to be consistent with EBSD map in Fig. 1 with
 280 TD \parallel x axis, RD \parallel y axis and ND \parallel z axis.



281 **Fig. 4 Microstructure of oxide regions 1 using SPED.** **a** Correlation index map with
 282 overlaid monoclinic oxide grain boundaries shown in black (interphase boundaries shown in
 283 green). **b** Phase map with phase reliability values less than 10 shown as non-indexed points
 284 coloured according to legend below (**b**). **c** Monoclinic ZrO₂ orientation map coloured
 285 according to degrees away from the $\{106\}$ pole according to colour legend in (**d**). **d**
 286 Normalised frequency of orientations and pole figure with respect to degrees away from the
 287 main texture component $\{106\}_{m\text{-ZrO}_2}$ for both EBSD and SPED data. Denoted with pink
 288 disks and blue crosses are possible theoretical orientation relationships $\{111\} \langle$
 289 $101 \rangle_{m\text{-ZrO}_2} \parallel \{101\} \langle 112 \rangle_{t\text{-ZrO}_2} \parallel \{0002\} \langle 1120 \rangle_{\text{Zr}}$ and $\{111\} \langle$
 290 $101 \rangle_{m\text{-ZrO}_2} \parallel \{0002\} \langle 1120 \rangle_{\text{Zr}}$, respectively.

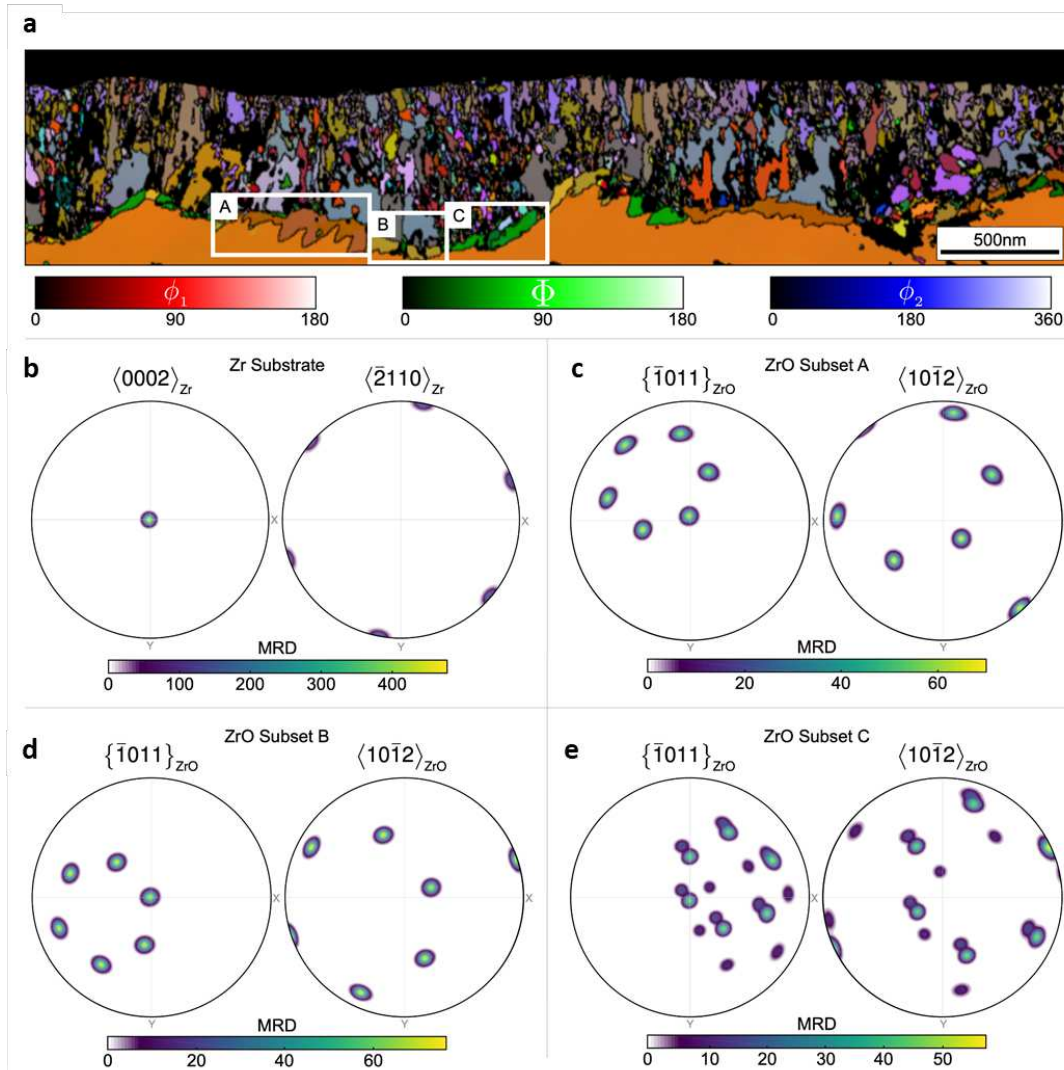


292
 293
 294
 295
 296
 297
 298
 299
 300
 301

Fig. 5 Microstructure of oxide regions 2 using SPED. **a** Correlation index map with overlaid monoclinic oxide grain boundaries shown in black (interphase boundaries shown in green). **b** Phase map with phase reliability values less than 10 shown as non-indexed points coloured according to legend below **(b)**. **c** Monoclinic ZrO₂ orientation map coloured according to degrees away from the $\{11\bar{2}\}$ pole according to colour legend in **(d)**. **d** Normalised frequency of orientations and pole figure with respect to degrees away from the main texture component $\{11\bar{2}\}_{m-ZrO_2}$ for both EBSD and SPED data. Denoted with orange disks and red crosses are the major and minor theoretical orientation $\{11\bar{2}\} < 111 >_{m-ZrO_2}$ || $\{0002\} < 1\bar{1}00 >_{Zr}$ and $\{31\bar{2}\} < 111 >_{m-ZrO_2}$ || $\{0002\} < 1\bar{1}00 >_{Zr}$.

302 Fig. 5a shows the SPED correlation index map from within region 2, where the oxide
 303 exhibits a complex microstructure consisting of narrow columnar grains and regions of
 304 equiaxed nanostructured oxide, with a smaller average grain width of ~ 41 nm when
 305 compared to region 1. The SPED phase map in Fig. 5b shows that the majority of the oxide in
 306 this region is also composed of the monoclinic ZrO_2 phase. The tetragonal phase fraction is
 307 less than 1% and is mainly confined to small, isolated equiaxed grains. There are also some
 308 isolated larger grains at the metal-oxide interface which are indexed as hexagonal ZrO sub-
 309 oxide phase in agreement with previous observations⁵⁵. Fig. 5c and d show the m-ZrO₂
 310 orientation map, coloured as degrees away from the $\{11\bar{2}\}$ main texture component, and the
 311 corresponding normalised frequency of orientations compared with that from EBSD. Most of
 312 the monoclinic oxide grains are oriented between 0° and 35° away from the $\{11\bar{2}\}$ pole with
 313 a peak of orientations at about 10° . As expected, the SPED data exhibits a larger spread
 314 compared to the EBSD data due to the smaller number of oxide grains sampled. The SPED
 315 $\{11\bar{2}\}$ pole figure, also coloured as degrees away from the main texture component $\{11\bar{2}\}$
 316 and overlaid with the orientations from the theoretical orientation relationships calculated
 317 based on the orientation of the metal in the SPED data, confirm the presence of these two
 318 monoclinic texture components. We also observe a slightly larger misalignment between the
 319 experimental and the theoretical data compared to that in the EBSD measurement. The
 320 theoretical peaks of the $\{11\bar{2}\}$ are very close to those obtained using both SPED and EBSD as
 321 seen in Fig. 5d. **Error! Reference source not found.** Additionally, the SPED technique
 322 allows us to investigate the potential role of the ZrO sub-oxide on the oxide texture. In region
 323 1, the suboxide forms an almost continuous layer between the metal substrate and the ZrO_2
 324 film, demonstrating the characteristic ‘sawtooth’ sub-oxide morphology⁵⁵ as seen in Fig. 4b.
 325 On the other hand, fewer isolated grains were observed in region 2. Further analysis showed
 326 that an orientation relationship between the metal and the ZrO phase exists in region 1 but not
 327 in region 2. Fig. 6a shows the SPED orientation map coloured according to Euler angles for
 328 all major phases formed in region 1. The oxide has been split into subsets A, B and C in Fig.
 329 6a, which cover the three main sub-oxide orientations observed in this region. Contoured
 330 $\{0002\}$ and $\langle\bar{2}110\rangle$ pole figures for the Zr substrate and $\{\bar{1}011\}$ and $\langle 10\bar{1}2\rangle$ pole figures
 331 for the different ZrO sub-oxide regions are shown in Fig. 6b-e, where the substrate $\{0002\}$
 332 pole is aligned with the ‘z’ direction of the pole figure in order to better visualise any
 333 orientation relationships. The pole figures show that in subset A and B, the sub-oxide follows
 334 the main orientation relationship identified in⁵⁶, with $\{0002\}_{\text{Zr}} \parallel \{\bar{1}011\}_{\text{ZrO}}$ and
 335 $\langle\bar{2}110\rangle_{\text{Zr}} \parallel \langle 10\bar{1}2\rangle_{\text{ZrO}}$. This is also in agreement with TEM observations of sub-oxide
 336 formation during in-situ annealing⁵⁷. In subset C, the orientation relationship is less clear, as
 337 this region is composed of two distinct sub-oxide orientations, however both of them are also
 338 close to the major orientation relationship reported previously^{56,57}.

339



340

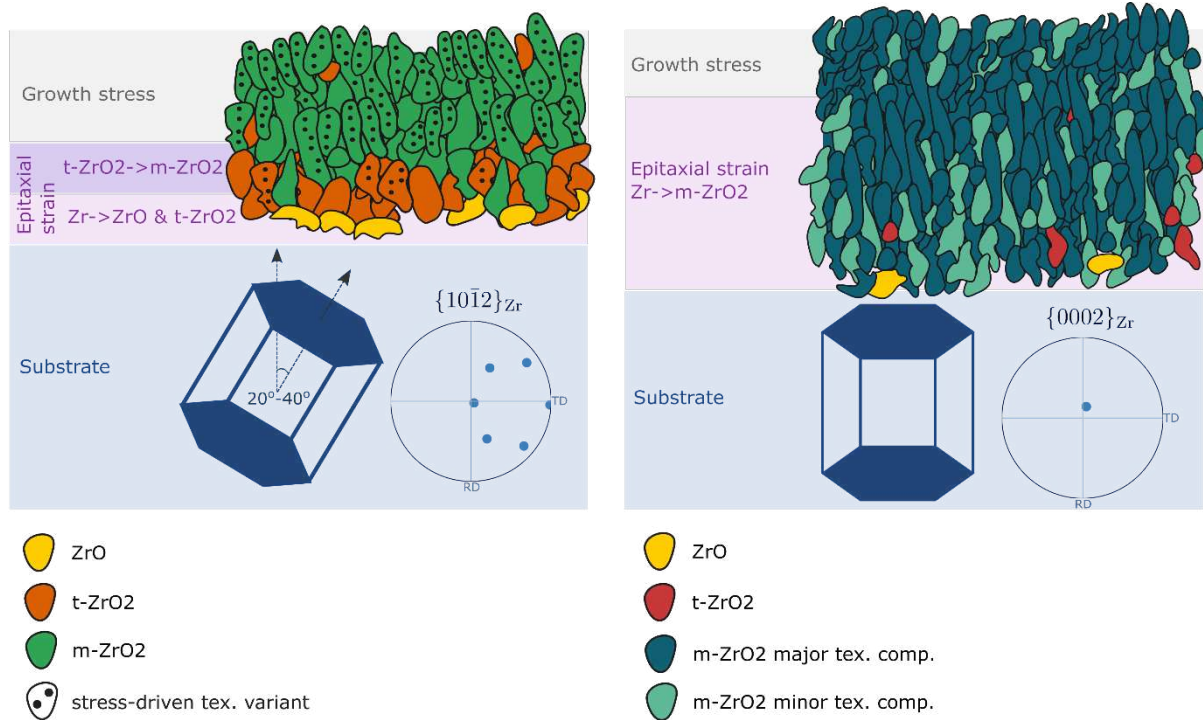
341 **Fig. 6 Sub-oxide orientation in oxide region 1.** **a** SPED orientation map for hexagonal ZrO
 342 and hexagonal Zr from region 1 in Euler angle colouring as shown in legend. **b** Contoured
 343 $\{0002\}$ and $\langle \bar{2}110 \rangle$ pole figures for the Zr substrate. **c-e** Contoured $\{\bar{1}011\}$ and $\langle 10\bar{1}2 \rangle$
 344 pole figures for the different ZrO sub-oxide subsets labelled in (a). The $\{0002\}_{\text{Zr}}$ is aligned
 345 parallel to the pole figure z direction to make orientation relationships clearer.

346 Discussion

347 Detailed analysis over significant length scales shows that the orientation of Zr metal grains
 348 has a dramatic effect on the subsequent development of the local oxide nanostructure and
 349 texture, and thus the local protectiveness of the oxide. This has wide-reaching implications
 350 for the understanding of oxide nucleation and growth processes, and also highlights the
 351 importance of multiscale characterisation and correlative microscopy in understanding these
 352 complex processes. In the present case, focusing on two oxide regions separated by about 10
 353 mm, identical material and corrosion conditions resulted in marked differences in oxide
 354 protectiveness, which seems to be strongly correlated to differences in the orientation of the
 355 underlying metal grains. Our findings contradict the common belief that in single-phase Zr
 356 alloys with split-basal texture, substrate orientation has little influence on the oxide texture³¹.

a

b



358 **Fig. 7. Schematic representation of the mechanisms of Zr metal to oxide transformation**
 359 **and their effect on the grain morphology and texture of the oxide film based on the**
 360 **orientation of the substrate metal grain.** Two types of oxide microstructure are observed
 361 based on the orientation of the substrate grain. **a** Region 1: a protective oxide layer with long
 362 columnar grains and low energy grain boundaries under the influence of the growth stress. **b**
 363 Region 2: less protective oxide, thicker and with more disordered smaller grains. In **(a)** ZrO,
 364 t-ZrO₂ and m-ZrO₂ grains are shown in yellow, orange and green, respectively, and dots
 365 indicate stress-driven texture variant; in **(b)** ZrO, t-ZrO₂ and m-ZrO₂ grains are shown in
 366 yellow, orange and green, respectively, where darker and lighter shade of green indicates the
 367 major and minor m-ZrO₂ texture components.

368 The schematic in Fig. 7 summarises our findings for the competing mechanisms of
 369 oxide nucleation and growth. In a typical metal grain in split-basal textured single-phase Zr
 370 alloys, the c-axis of the hcp crystal is positioned at 20° to 40° away from the outer surface
 371 normal, and so pyramidal planes with Miller indices $\{h0il\}$ are close to parallel to the outer
 372 surface (Fig. 7a). In contrast, these alloys also contain a smaller fraction of grains with basal
 373 planes close to parallel to the outer surface, represented in Fig. 7b. According to our
 374 observations, the former substrate grain type forms a thinner oxide film with wider and more
 375 columnar grains, with higher fraction of metastable ZrO and tetragonal ZrO₂ phases,
 376 compared to the latter. In both cases, the majority of the oxide consists of monoclinic ZrO₂,
 377 however, with a strong one-component epitaxial texture in the first case, and a two-
 378 component epitaxial texture in the second case.

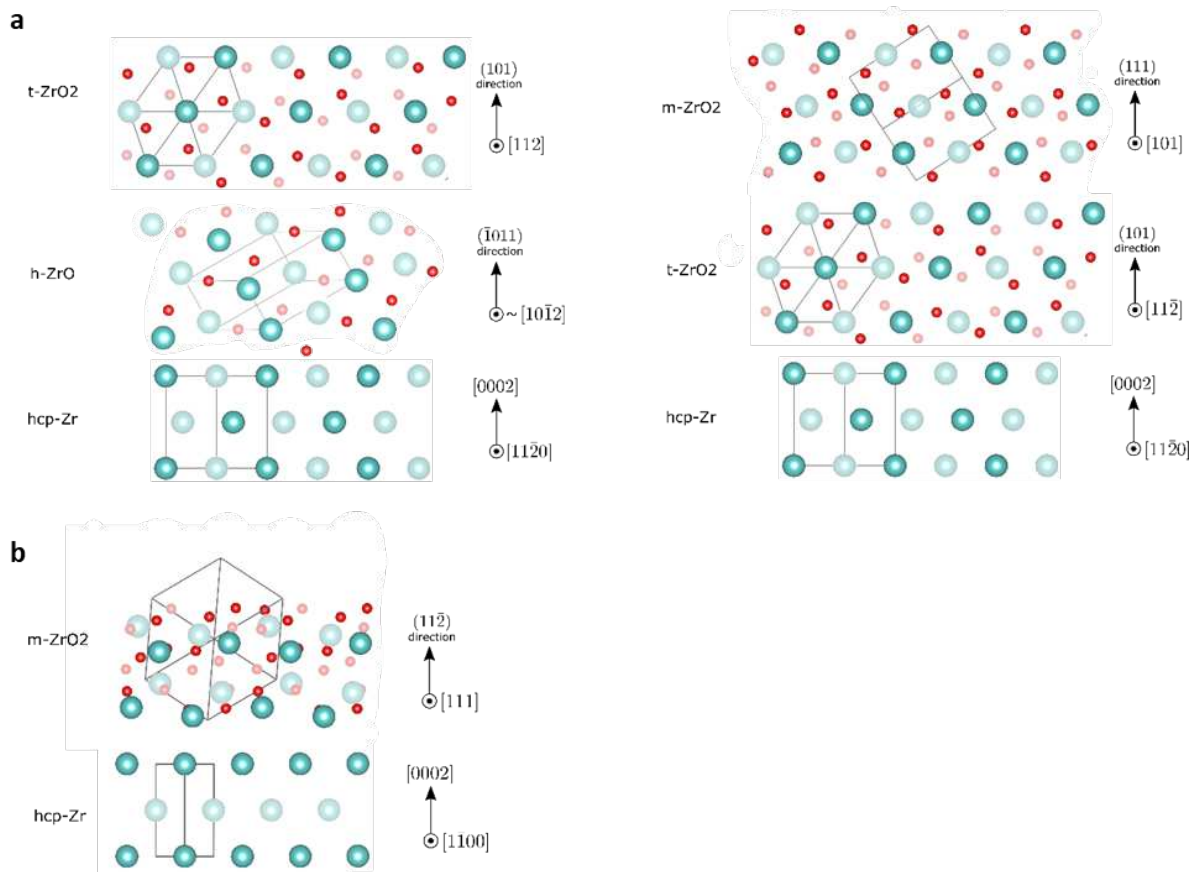
379 We now discuss how the crystallographic orientation of the metal grain influences the
 380 formation of these oxide microstructures. Since the basal plane is the most densely packed
 381 and the lowest energy plane in the hcp Zr lattice, it is expected to be the most corrosion
 382 resistant. The pyramidal plane $\{h0il\}$ orientations are expected to exhibit properties in
 383 between those of the basal and the prism orientations as they lie on an energetically favoured
 384 region in the surface energy anisotropy projection with a minimum at the basal orientation
 385 $\{0002\}$ and a maximum at the prism orientation $\{10\bar{1}0\}$, as calculated by a broken-bond

386 based geometric model⁵⁸. Multiple experimental and theoretical studies^{7,23,59} on single
 387 crystal Zr have shown that the prismatic planes oxidise more readily in water and in pure
 388 oxygen than the basal plane with an estimated oxygen diffusion twice as fast along the
 389 $[10\bar{1}0]$ direction compared to the $[0002]$ direction. Nevertheless, based on our FIB cross
 390 section analysis, the ‘split-basal’ orientations showed a corrosion rate two times lower than
 391 that of the basal-type orientations. A similar result was reported for Ni^{12,14}, where under
 392 certain thermodynamic conditions, the corrosion rate did not follow the surface energy
 393 anisotropy of face-centred cubic metals. Instead, the formation of a passivating oxide film
 394 slowed down the corrosion rate on certain surfaces, and the surfaces most susceptible to
 395 corrosion were found to be those most able to form a protective film¹². In the present case,
 396 that effect can be attributed to the competition between the epitaxial strain, i.e. the lattice
 397 matching, and the growth stress in the nucleation and growth stages of oxide formation. A
 398 charge-optimized many-body potential study by Noordhoek et al.²⁶ demonstrated that water
 399 dissociates faster, and that atomic O and H diffuse further into the prism planes with a more
 400 even distribution compared with the basal plane—87% of O was found to lie between the top
 401 two layers for $\{0002\}$, compared to 54% and 44% for $\{11\bar{2}0\}$ and $\{10\bar{1}0\}$, respectively.
 402 Therefore, oxygen atoms will be more evenly distributed and penetrate to a greater depth in
 403 substrate orientations close to the ideal split-basal texture, such as that in region 1. That
 404 would lead to a higher fraction of oxygen vacancies in the same volume of material, and
 405 hence, favour the formation of the lower-stoichiometry ZrO phase and the vacancy-stabilised
 406 tetragonal ZrO₂ phase, when compared with the basal orientation that corresponds to region
 407 2.

408 Both types of Zr grains oxidise by strong alignment of the child oxide phase with the
 409 parent metal phase according to specific epitaxial orientation relationships. In the case of a
 410 grain with a ‘split-basal’ orientation, it was previously thought that no single orientation
 411 relationship exists between the metal and the oxide³¹. We identified for the first time that the
 412 orientation of the metal grain energetically favours the nucleation of tetragonal ZrO₂ based on
 413 the epitaxial relationship $\{101\} \langle 11\bar{2} \rangle_{t\text{-ZrO}_2} \parallel \{0002\} \langle 11\bar{2}0 \rangle_{\text{Zr}}$, and in some cases
 414 hexagonal ZrO based on the epitaxial relationship $\{\bar{1}011\} \langle 10\bar{1}2 \rangle_{\text{ZrO}} \parallel \{0002\} \langle$
 415 $11\bar{2}0 \rangle_{\text{Zr}}$. And so, when the sub-oxide ZrO phase does form, it can transform to tetragonal
 416 ZrO₂, maintaining the same tetragonal texture as that of the grains directly nucleated from the
 417 Zr metal. Lattice matching also drives the tetragonal to monoclinic phase transformation
 418 based on the relationship $\{111\} \langle 10\bar{1} \rangle_{m\text{-ZrO}_2} \parallel \{101\} \langle 11\bar{2} \rangle_{t\text{-ZrO}_2}$. We note that these
 419 three orientation relationships can be combined as $\{111\} \langle 10\bar{1} \rangle_{m\text{-ZrO}_2} \parallel \{101\} \langle$
 420 $11\bar{2} \rangle_{t\text{-ZrO}_2} \parallel \{\bar{1}011\} \langle 10\bar{1}2 \rangle_{\text{ZrO}} \parallel \{0002\} \langle 11\bar{2}0 \rangle_{\text{Zr}}$. In contrast, we have shown that
 421 a Zr metal grain with the c-axis normal to the interface, is more likely to directly nucleate as
 422 monoclinic ZrO₂, with $\langle 111 \rangle_{m\text{-ZrO}_2} \parallel \langle 1\bar{1}00 \rangle_{\text{Zr}}$ and $\{11\bar{2}\}_{m\text{-ZrO}_2} \parallel \{0002\}_{\text{Zr}}$ or
 423 $\{31\bar{2}\}_{m\text{-ZrO}_2} \parallel \{0002\}_{\text{Zr}}$.

424 Fig. 8 shows the atomic structures of the interfaces between the metal and oxide
 425 phases in the two types of regions, and Table 1 lists the epitaxial strains required between
 426 phase transformations, calculated according to the Zr-Zr distance within the corresponding
 427 crystal structure. We note that there is no significant difference in the total epitaxial strains in
 428 the two regions when we consider the transformations from Zr metal to monoclinic ZrO₂.
 429 Therefore, we need to consider the effect of growth stresses on the oxidation process, which
 430 is determined by a combination of the effect of areal footprint of the symmetry variant and
 431 the crystal stiffness anisotropy of the child phase^{29,35}. The child phase variants formed from

432 different parent symmetry operators will have different areal footprints on the outer surface
 433 based on the orientation of the parent crystal. For example, when the Zr basal pole is parallel
 434 to ND, the symmetry variants would have the same footprint, whereas when it is positioned at
 435 an angle to ND, these will differ. The epitaxial strains necessary to form a coherent interface
 436 between the two lattices, on the other hand, would stay the same—the atomic interface is the
 437 same but rotated with respect to the global (sample) coordinate system. And so, in region 1,
 438 we would have an inequivalent distribution of areal footprints and stiffnesses, some of which
 439 will be favourable for growth based on minimising the stresses and with most of the volume
 440 change accommodated normal to the metal-oxide interface³⁶. On the other hand, in region 2,
 441 the epitaxial strains remain strong and drive all symmetry variants to grow in equal
 442 proportion.



443

444 **Fig. 8. Atomic structure of interface.** Schematic of the interfaces formed based on the
 445 identified orientation relationships. **a** Region 1: $\{101\} \langle 11\bar{2} \rangle_{t\text{-ZrO}_2} \parallel \{\bar{1}011\} \langle 10\bar{1}2 \rangle_{h\text{-ZrO}} \parallel \{0002\} \langle 11\bar{2}0 \rangle_{\text{hcp-Zr}}$ (left) and $\{111\} \langle 10\bar{1} \rangle_{m\text{-ZrO}_2} \parallel \{101\} \langle 11\bar{2} \rangle_{t\text{-ZrO}_2} \parallel \{0002\} \langle 11\bar{2}0 \rangle_{\text{hcp-Zr}}$ (right). **b** Region 2: $\{11\bar{2}\} \langle 111 \rangle_{m\text{-ZrO}_2} \parallel \{0002\} \langle 1\bar{1}00 \rangle_{\text{hcp-Zr}}$. Two atomic planes shown in the out-of-page direction, where shade indicates the atom's relative distance and darker atoms are closer to the reader. Blue and red spheres represent Zr and O atoms, respectively. Produced using VESTA⁶⁰.

451

452 Based on the epitaxial relationships in region 1, the nucleated tetragonal variants will
 453 have either the $\{001\}$ or the $\{110\}$ plane close to parallel to the outer surface, which then
 454 transform to $\{10\bar{6}\}$ and $\{100\}$ in the monoclinic phase, respectively. Previously, preferential
 455 growth of the $\{001\}_{t\text{-ZrO}_2}$ and the $\{10\bar{6}\}_{m\text{-ZrO}_2}$ was attributed to their small areal footprint

456 as a determining factor that minimises the compressive stress²⁹. However, these orientations
 457 have very similar areal footprints—26.0 Å² and 26.4 Å² for {001}_{t-ZrO₂} and {110}_{t-ZrO₂},
 458 and 27.3 Å² and 27.9 Å² for {10 $\bar{6}$ }_{m-ZrO₂} and {100}_{m-ZrO₂}, respectively. **Error! Reference**
 459 **source not found.**a shows the directional dependence of Young’s modulus in the body-
 460 centred tetragonal ZrO₂ crystal, which suggests the {001}_{t-ZrO₂} has a lower stiffness
 461 compared to {110}_{t-ZrO₂}. Thus, the growth of the {001}_{t-ZrO₂} variants, which subsequently
 462 transform to {10 $\bar{6}$ }_{m-ZrO₂}, would minimise the growth stress in the oxide film. These results
 463 agree with previous studies, which have reported similar monoclinic oxide textures of {10 \bar{l} }
 464 (where $l = 2, 3, 4$)⁶¹⁻⁶⁴. The particular value of l will depend on the metal grain orientation
 465 that the oxide has transformed from. Importantly, our results show that the tetragonal phase is
 466 a required precursor to the monoclinic phase, in order for a protective oxide layer to form
 467 with a strong single-footprint epitaxial texture consisting of wider and more columnar grains.
 468 The sub-oxide was found not to influence the oxidation significantly and is therefore more
 469 likely a byproduct of slow oxidation, as suggested previously^{47,65}. These stronger textured
 470 oxides are likely to have a higher fraction of protective, low angle grain boundaries, and also
 471 coarser, more coherent microstructures as it was previously shown that columnar grain
 472 growth is terminated by small mismatches between local grain orientations⁶⁶.

473 In contrast to our findings, the tetragonal to monoclinic phase transformation was
 474 thought previously to cause cracking in the oxide layer, and thus have a mainly negative role
 475 on the oxidation process³⁴. We need to point out that there are different mechanisms of
 476 tetragonal phase stabilisation—chemically stabilised grains due to alloying elements such as
 477 Sn, and stress stabilised grains might be allowed to grow larger and therefore destabilise the
 478 oxide when they transform. Tetragonal grains stabilised throughout the oxidation process,
 479 whether due to small size or vacancies, are likely to have a beneficial effect by allowing for
 480 the formation a coherent and protective microstructure. Another potential contributing factor
 481 to the more protective oxide in region 1 is that the metastable phases allow a more gradual
 482 volume expansion from metal to oxide, and so fewer defects develop in the oxide
 483 microstructure leading to lower local corrosion rates. The volume strain necessary to
 484 transform Zr to ZrO is 11.9%, the strain to transform ZrO to tetragonal ZrO₂ is 29.3% and the
 485 expansion from tetragonal to monoclinic ZrO₂ is 5.9%, as opposed to a sudden expansion of
 486 53.3% from Zr to monoclinic ZrO₂, as occurs in region 2.

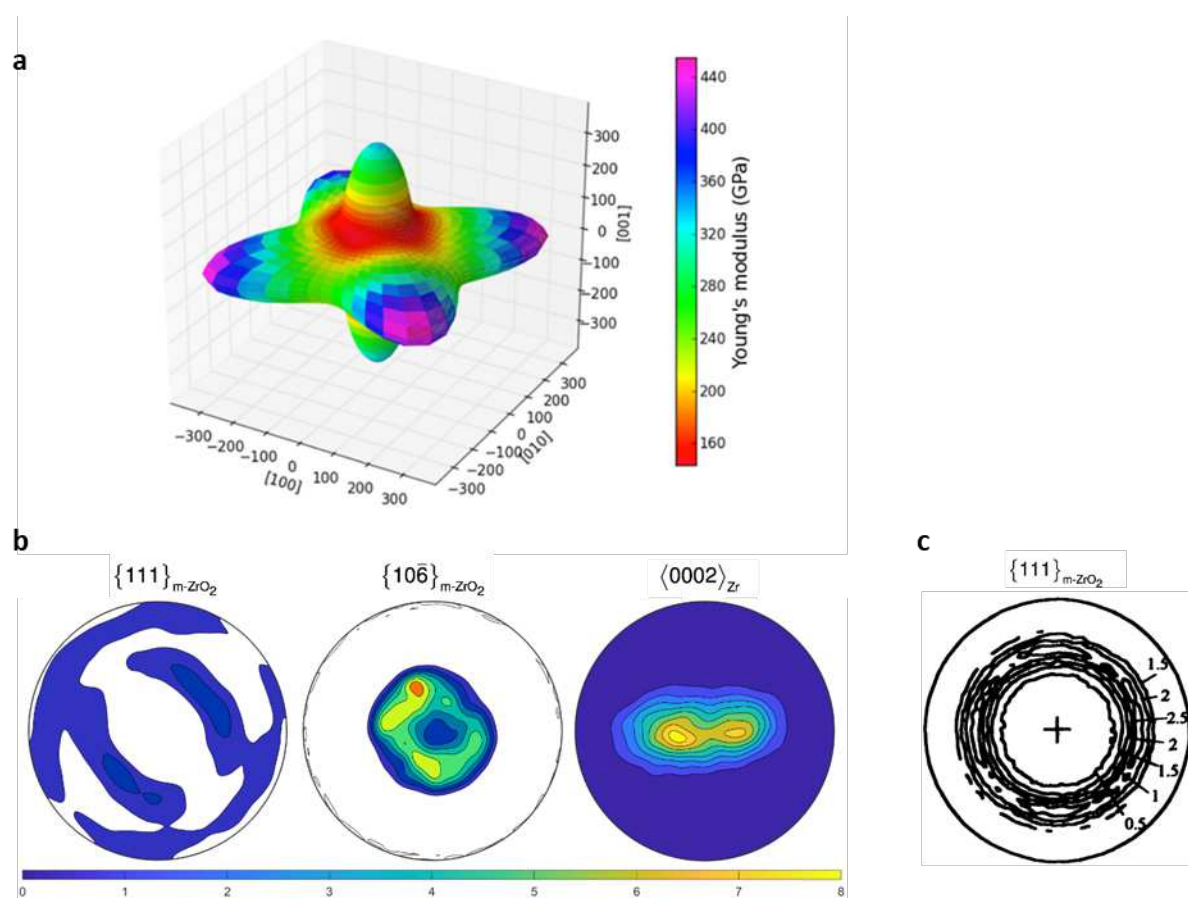
487 Both orientation relationships in region 2 form an oxide with a single unique areal
 488 footprint—the {11 $\bar{2}$ }_{m-ZrO₂} with a footprint of 31.5 Å² or the {31 $\bar{2}$ }_{m-ZrO₂} plane with a
 489 footprint of 32.1 Å², since they are both formed from a metal grain with the basal plane
 490 normal to the oxide growth direction. The similar footprints, and potentially similar
 491 stiffnesses of the two orientations, leads to the epitaxial strain, rather than the growth stress,
 492 being the stronger mechanism, driving the growth of both texture components with a higher
 493 prevalence of the {11 $\bar{2}$ }_{m-ZrO₂} orientation. It is the simultaneous growth of two epitaxial
 494 texture components in combination with the direct transformation from Zr metal to
 495 monoclinic ZrO₂ that most likely enhances oxygen ion transport through the oxide as the
 496 elongated oxide grains are not so well organised and more high-angle grain boundaries are
 497 formed reducing the level of passivation.

498 **Table 1. Epitaxial strains.** Calculated based on the difference between the Zr-Zr distances in
 499 the corresponding lattices. Shear is ignored.

500

	Phase transformation	In-plane strains (%)	Average in-plane strain (%)	Average out-of-plane strain (%)
Reg. 1	hcp-Zr -> h-ZrO	6.6, -5.4	0.6	0.6
	hcp-Zr -> t-ZrO ₂	10.1, 11.0	10.6	12.0
	h-ZrO -> t-ZrO ₂	3.8, 15.5	9.7	11.5
	t-ZrO ₂ -> m-ZrO ₂	-	1.4	-0.6
Reg. 2	hcp-Zr -> m-ZrO ₂	-	11.8	11.5

501



502

503 **Fig. 9 Young's modulus of t-ZrO₂ and modelled macrotexture.** **a** Directional dependence
504 of Young's modulus in the body-centred tetragonal ZrO₂ crystal. **b** Contoured pole figures for
505 the {111} and {10 $\bar{6}$ } monoclinic ZrO₂ poles as modelled using the orientation relationships
506 obtained in this study based on Zircaloy-4 substrate with EBSD texture shown in the {0002}
507 Zr contour pole figure. **c** Measured monoclinic ZrO₂ {111} contour pole figure from a 14 μ m
508 thick oxide film formed in 400° steam on Zircaloy-4 by Parise⁶⁷.

509 Moreover, we considered the oxide texture that would result due to a transformation of
510 a large number of metal grains present in a typical sample with split-basal texture. The results
511 are shown in **Error! Reference source not found.**, where all metal orientations with a basal

512 pole within 20° of ND were assumed to transform according to the orientation relationships
513 in region 2, and the remaining metal orientations were assumed to transform according to the
514 orientation relationships in region 1 with a preferential growth of the oxide orientations
515 closest to $\{10\bar{6}\}_{m-ZrO_2}$. The monoclinic oxide $\{111\}$ contour pole figure shows a close to
516 uniform distribution, which agrees well with the measured $\{111\}$ pole figure by Parise⁶⁷ in
517 **Error! Reference source not found.** (B). Combined with the result for the $\{10\bar{6}\}_{m-ZrO_2}$
518 pole figure, it can be seen how the macrotexture of the oxide appears to have a preferential
519 fibre. However, this macrotexture is formed by a large number of epitaxial textured oxide
520 grains formed from metal grains with different orientations. Our study demonstrates that
521 there is a clear epitaxial orientation relationship determining the oxide orientations, and it is
522 incorrect to describe the oxide crystallographic texture as ‘fibre’ texture.

523 In summary, this work demonstrates the importance of the substrate orientation on the
524 corrosion protectiveness of the oxide and the complex interplay between the two mechanisms
525 of epitaxial strain and growth stress on that process. In engineering alloys, which experience
526 inward corrosion and a Pilling-Bedworth ratio of more than one, epitaxial strain due to a
527 lattice matching between the substrate and the oxide drives a more disorderly growth of the
528 nanostructure oxide and therefore less protection. The growth stress, on the other hand,
529 achieves a more well-ordered, coarser oxide microstructure and improved global corrosion
530 performance. This finding opens the possibility for improved corrosion performance of a
531 large range of alloys through optimisation of their processing route.

532 **Methods**

533 **Material selection**

534 The material used in this study was sheet Zircaloy-2 material in the recrystallised condition
535 with average equiaxed grain diameter of ~35.9 µm and chemical composition within the
536 range defined in ASTM B353. The coupon was subjected to corrosion testing for 46 days at
537 350°C in simulated pressurised water reactor (PWR) chemistry as part of a large-scale testing
538 program⁶⁸, forming an average oxide thickness of ~1.2 µm as estimated from weight gain
539 data.

540 **Sample Preparation**

541 In order to reduce the topography inherent to oxidised zirconium alloys and to remove the
542 outer portion of equiaxed grains related to the fast initial oxidation process³⁹, a 2 x 2 mm
543 section of the oxidised Zircaloy-2 sample was prepared using 4000 grit silicon carbide paper
544 with a final polish in 0.06 µm colloidal silica. A total of ~0.4 µm of oxide was removed, as
545 measured by subsequent cross-sectional measurements. EBSD analysis was performed on
546 this surface as discussed below. Following EBSD analysis, two TEM liftouts were made from
547 different areas of the prepared oxide surface using the in situ liftout technique with an FEI
548 Quanta 3D focused ion beam (FIB) instrument. These samples were thinned to electron
549 transparency for SPED analysis using the standard FIB procedure with a final low energy
550 cleaning step. The position of these liftouts is shown in Fig. 1b.

551 In order to evaluate the local oxide thickness, trenches were prepared in different oxide
552 regions using the same FIB instrument. The oxide surface was firstly protected using Pt, a
553 regular cross section pattern was then used to mill out a region of the oxide and underlying
554 metal using an accelerating voltage of 30 KeV and a current of 3 nA. A final polish was
555 performed on the cross-sectional surface at 1 nA in order to provide a clean surface for

556 accurate oxide thickness measurement. Secondary electron imaging was performed at 5 KeV
557 with a current of 1.6 nA.

558 The remaining oxide was then carefully removed using 0.06 μm colloidal silica. The material
559 removal rate was relatively slow to ensure that significant amounts of the Zr substrate were
560 not removed. Once the oxide was removed, the underlying metal microstructure was assessed
561 with a further EBSD map (details below), using trenches as fiducial markers to match the
562 metal and oxide locations.

563 **Electron backscatter diffraction**

564 In order to obtain reliable bulk EBSD analysis of nanograined materials such as ZrO_2 , it is
565 vital that the interaction volume of the electron beam is minimised. In the present case this is
566 achieved with a low accelerating voltage of 10 KeV and a current of 1.6 nA using an FEI
567 Magellan 400 XHR Field Emission Gun Scanning Electron Microscope (FEG-SEM). The
568 unique column design on this microscope allows for a high current density to be maintained
569 in a small spot size in order to get sufficient signal out of the sample at low accelerating
570 voltages/currents. The disadvantage of using such beam conditions is that the backscatter
571 signal on the detector is relatively weak. This is overcome by the use of the high-resolution
572 Oxford Instruments Nordlys Nano 2 EBSD detector, operated at ~ 7 Hz, using 4 x 4 binning.
573 For the oxide measurement, a total area of 50 x 50 μm^2 was measured with a step size of 100
574 nm, with a total acquisition time of ~ 24 hours. The patterns were indexed using the Oxford
575 Instruments Aztec software suite with an indexing rate of ~ 60 %. Due to the small oxide
576 grain size, each indexed point in the map most likely corresponds to a unique oxide grain. It
577 should be pointed out here that there are small ~ 5 μm squares in the orientation map that
578 appear to show a different crystallographic texture. These are regions of intentional focused-
579 ion-beam (FIB) damage that formed part of another study⁴⁹, and are excluded from this
580 analysis.

581 After oxide removal, a second EBSD map was obtained from the underlying metal. Due to
582 the relatively large grain size, an accelerating voltage of 30 keV was used with a current of
583 3.2 nA using the same microscope and detector set up as used for the oxide EBSD. Patterns
584 were acquired with 8 x 8 binning over a total area of 100 x 100 μm . A 250 nm step size was
585 used at a speed of ~ 70 Hz giving a total acquisition time of 40 minutes. As with the oxide
586 map, the patterns were indexed using the Oxford Instruments Aztec software suite with an
587 indexing rate of ~ 80 %. All EBSD data was analysed using the Channel 5 software suite
588 developed by Oxford Instruments and the open-source MATLAB toolbox MTEX⁶⁹. A
589 similar number of indexed points in all regions were analysed for a more accurate texture
590 comparison.

591 **Scanning precession electron diffraction**

592 In order to analyse the local microstructure and microtexture in different oxide regions in
593 more detail, scanning precession electron diffraction was performed on the two FIB liftouts
594 from regions 1 and 4 in Fig. 1 (B). SPED phase and orientation maps were acquired using a
595 Tecnai TF30 transmission electron microscope operated at 300 KeV fitted with a Nanomegas
596 ASTAR SPED system. The patterns were acquired at 25 frames per second with a step size of
597 5 nm and a precession angle of 0.4 degrees and indexed offline using the ASTAR template
598 matching procedure⁵⁴. Orientations and phases identified with a reliability index less than 10
599 were excluded from the analysis, more details on these criteria can be found in ref.⁷⁰. The
600 grain size is estimated using the linear intercept method from the resultant grain boundary
601 maps, with grain boundaries defined by a critical misorientation threshold of 5° . Although the

602 analysis of the entire oxide thickness is not possible due to removal of the outer portion of
603 oxide, an accurate measurement of the grain widths in the inner oxide can be performed.

604 **Oxide texture modelling**

605 A Python code was developed in order to model the oxide texture formed on the observed
606 substrate orientations. The raw EBSD orientation data was used to find the theoretical child
607 phase orientations for a given orientation relationship between metal and oxide or between
608 two oxide phases. The epitaxial relationships were found by starting with the substrate
609 orientation, generating a large number of possible oxide orientations by incremental rotation
610 of the oxide lattice in 3° intervals until a match between the theoretical and experimental
611 equal-area-projection pole figures was found. Then, the smallest Miller indices planes for
612 these orientations was calculated within a 10° tolerance. The misalignment between the
613 theoretical and the experimental spots are most likely a result of combination of factors
614 including error in the orientation measurement of the metal grain (e.g. some distortion in the
615 sample when the oxide is polished off), the undulated interface between the metal and the
616 oxide, and internal misorientation in the metal grain.

617

618 **References**

- 619 1. Koch, G. Cost of corrosion. in *Trends in Oil and Gas Corrosion Research and*
620 *Technologies: Production and Transmission* 3–30 (Elsevier Inc., 2017).
621 doi:10.1016/B978-0-08-101105-8.00001-2
- 622 2. Fushimi, K., Miyamoto, K. & Konno, H. Anisotropic corrosion of iron in pH 1
623 sulphuric acid. *Electrochim. Acta* **55**, 7322–7327 (2010).
- 624 3. Horton, D. J., Zhu, A. W. & Scully, J. R. Crystallographic controlled dissolution and
625 surface faceting in disordered face-centered cubic FePd. *MRS Commun.* **4**, 113–119
626 (2014).
- 627 4. Bland, L. G., Gusieva, K. & Scully, J. R. Effect of Crystallographic Orientation on the
628 Corrosion of Magnesium: Comparison of Film Forming and Bare Crystal Facets using
629 Electrochemical Impedance and Raman Spectroscopy. *Electrochim. Acta* **227**, 136–
630 151 (2016).
- 631 5. Yasuda, M., Weinberg, F. & Tromans, D. Pitting Corrosion of Al and Al-Cu Single
632 Crystals. *J. Electrochem. Soc.* **137**, 3708–3715 (1990).
- 633 6. Davis, B. W., Moran, P. J. & Natishan, P. M. Metastable pitting behavior of aluminum
634 single crystals. *Corros. Sci.* **42**, 2187–2192 (2000).
- 635 7. Kim, H. G., Kim, T. H. & Jeong, Y. H. Oxidation characteristics of basal (0002) plane
636 and prism (1120) plane in HCP Zr. *J. Nucl. Mater.* **306**, 44–53 (2002).
- 637 8. Muller, M. & Oechsner, H. In situ STM and AES studies on the oxidation of Cr(110).
638 *Surf. Sci.* **387**, 269–278 (1997).
- 639 9. Cathcart, J. V., Petersen, G. F. & Sparks, J. C. J. The Structure of Thin Oxide Films
640 Formed on Nickel Crystals. *J. Electrochem. Soc.* **116**, 664 (1969).
- 641 10. Li, H., Czerwinski, F., Zhilyaev, A. & Szpunar, J. A. Computer modelling the
642 diffusion of Ni in NiO at high temperatures. *Corros. Sci.* **39**, 1211–1219 (1997).

- 643 11. Czerwinski, F. & Szpunar, J. A. Controlling the surface texture of nickel for high
644 temperature oxidation inhibition. *Corros. Sci.* **41**, 729–740 (1999).
- 645 12. Gray, J. J., Dasher, B. S. El & Orme, C. A. Competitive effects of metal dissolution
646 and passivation modulated by surface structure: An AFM and EBSD study of the
647 corrosion of alloy 22. *Surf. Sci.* **600**, 2488–2494 (2006).
- 648 13. Young, F. W. J., Cathcart, J. V & Gwathmeyf, A. T. The rates of oxidation of several
649 faces of a single crystal of copper as determined with elliptically polarized light. *Acta*
650 *Metall.* **4**, 145 (1956).
- 651 14. Schuh, C. A., Anderson, K. & Orme, C. Rapid assessment of anisotropic surface
652 processes: experiments on the corrosion of Inconel 600. *Surf. Sci.* **544**, 183–192
653 (2003).
- 654 15. Liu, M., Qiu, D., Zhao, M.-C. C., Song, G. & Atrens, A. The effect of crystallographic
655 orientation on the active corrosion of pure magnesium. *Scr. Mater.* **58**, 421–424
656 (2008).
- 657 16. Abayarathna, D., Hale, E. B., O’Keefe, T. J., Wang, Y. M. & Radovic, D. Effects of
658 sample orientation on the corrosion of zinc in ammonium sulfate and sodium
659 hydroxide solutions. *Corros. Sci.* **32**, 755–768 (1991).
- 660 17. Davepon, B., Schultze, J. W., Konig, U. & Rosenkranz”, C. R. Crystallographic
661 orientation of single grains of polycrystalline titanium and their influence on
662 electrochemical processes. *Surf. Coatings Technol.* **169**, 85–90 (2003).
- 663 18. Pemsler, J. P. Diffusion of oxygen in zirconium and its relation to oxidation and
664 corrosion. *J. Electrochem. Soc.* **105**, 315 (1958).
- 665 19. Ploc, R. A. A transmission electron diffraction study of ZrO₂ on α -Zr (0001). *J. Nucl.*
666 *Mater.* **110**, 59–64 (1982).
- 667 20. Bakradze, G., Jeurgens, L. P. H. & Mittemeijer, E. J. The different initial oxidation
668 kinetics of Zr(0001) and Zr(101–0) surfaces. *J. Appl. Phys.* **110**, (2011).
- 669 21. Methfessel, M., Hennig, D. & Scheffer, M. Trends of the surface relaxations, surface
670 energies, and work functions of the 41 transition metals. *Phys. Rev. B* **46**, 4816–4829
671 (1991).
- 672 22. Błóński, P. & Kiejna, A. Structural, electronic, and magnetic properties of bcc iron
673 surfaces. *Surf. Sci.* **601**, 123–133 (2007).
- 674 23. Chiang, T. W., Chernatynskiy, A., Noordhoek, M. J., Sinnott, S. B. & Phillpot, S. R.
675 Anisotropy in oxidation of zirconium surfaces from density functional theory
676 calculations. *Comput. Mater. Sci.* **98**, 112–116 (2015).
- 677 24. Zhang, J. M., Wang, D. D. & Xu, K. W. Calculation of the surface energy of hcp
678 metals by using the modified embedded atom method. *Appl. Surf. Sci.* **253**, 2018–2024
679 (2006).
- 680 25. Lillard, R. S., Wang, G. F. & Baskes, M. I. The role of metallic bonding in the
681 crystallographic pitting of magnesium. *J. Electrochem. Soc.* **153**, 358–364 (2006).
- 682 26. Noordhoek, M. J., Liang, T., Chiang, T.-W., Sinnott, S. B. & Phillpot, S. R.
683 Mechanisms of Zr surface corrosion determined via molecular dynamics simulations

- 684 with charge-optimized many-body (COMB) potentials. *J. Nucl. Mater.* **452**, 285–295
685 (2014).
- 686 27. Franchy, R. Â. Growth of thin, crystalline oxide, nitride and oxynitride films on metal
687 and metal alloy surfaces. *Surf. Sci. Rep.* **38**, 195–294 (2000).
- 688 28. Khoi, N. N., Smeltzer, W. W. & Embury, J. D. Growth and Structure of Nickel Oxide
689 on Nickel Crystal Faces. *J. Electrochem. Soc.* **122**, 1495–1503 (1975).
- 690 29. Li, H., Glavicic, M. & Szpunar, J. A. A model of texture formation in ZrO₂ films.
691 *Mater. Sci. Eng. A* **366**, 164–174 (2004).
- 692 30. Tenckhoff, E. A review of texture and texture formation in Zircaloy tubing. *Zircon.*
693 *Nucl. Ind. 5th Int. Symp. ASTM STP 754* 5–25 (1982).
- 694 31. Garner, A., Frankel, P., Partezana, J. & Preuss, M. The effect of substrate texture and
695 oxidation temperature on oxide texture development in zirconium alloys. *J. Nucl.*
696 *Mater.* **484**, 347–356 (2017).
- 697 32. Pilling, N. B. & Bedworth, R. E. The oxidation of metals at high temperatures. *J. Inst.*
698 *Met* **29**, 529–591 (1923).
- 699 33. Dunn, J. S. The high temperature oxidation of metals. *Proc. R. Soc. A Math. Phys.*
700 *Eng. Sci.* **111**, 203–209 (1926).
- 701 34. Wei, J. *et al.* The effect of Sn on autoclave corrosion performance and corrosion
702 mechanisms in Zr–Sn–Nb alloys. *Acta Mater.* **61**, 4200–4214 (2013).
- 703 35. Stringer, J. Stress generation and relief in growing oxide films. *Corros. Sci.* **10**, 513–
704 543 (1970).
- 705 36. Guerain, M., Duriez, C., Grosseau-Poussard, J. L. & Mermoux, M. Review of stress
706 fields in Zirconium alloys corrosion scales. *Corros. Sci.* **95**, 11–21 (2015).
- 707 37. Heuer, A. H. & Rühle, M. Overview no. 45. On the nucleation of the martensitic
708 transformation in zirconia (ZrO₂). *Acta Metall.* **33**, 2101–2112 (1985).
- 709 38. Zhou, G. & Yang, J. C. Initial oxidation kinetics of Cu(100), (110), and (111) thin
710 films investigated by in situ ultra-high-vacuum transmission electron microscopy. *J.*
711 *Mater. Res.* **20**, 1684–1694 (2005).
- 712 39. Garner, A. *et al.* The microstructure and microtexture of zirconium oxide films studied
713 by transmission electron backscatter diffraction and automated crystal orientation
714 mapping with transmission electron microscopy. *Acta Mater.* **80**, 159–171 (2014).
- 715 40. Qin, W., Nam, C., Li, H. & Szpunar, J. Tetragonal phase stability in ZrO₂ film formed
716 on zirconium alloys and its effects on corrosion resistance. *Acta Mater.* **55**, 1695–1701
717 (2007).
- 718 41. Nicholls, R. J. *et al.* Crystal Structure of the ZrO phase at zirconium/zirconium oxide
719 interfaces. *Adv. Eng. Mater.* (2014). doi:10.1002/adem.201400133
- 720 42. Barberis, P. Zirconia powders and Zircaloy oxide films: tetragonal phase evolution
721 during 400°C autoclave tests. *J. Nucl. Mater.* **226**, 34–43 (1995).
- 722 43. Zhou, B. X., Li, Q., Yao, M. Y., Liu, W. Q. & Chu, Y. L. Effect of water chemistry
723 and composition on microstructural evolution of oxide on Zr-alloys. *J. ASTM Int.* 360

- 724 (2009).
- 725 44. Sabol, G. P. ZIRLO – an alloy development success. *J. ASTM Int.* **2**, 1–22 (2005).
- 726 45. Davenport, A. J., Oblonsky, L. J., Ryan, M. P. & Toney, M. F. The structure of the
727 passive film that forms on iron in aqueous environments. *J. Electrochem. Soc.* **147**,
728 (2000).
- 729 46. Gong, W. *et al.* Grain morphology and crystal structure of pre-transition oxides formed
730 on Zircaloy-4. *Corros. Sci.* **74**, 323–331 (2013).
- 731 47. Ni, N. *et al.* How the crystallography and nanoscale chemistry of the metal/oxide
732 interface develops during the aqueous oxidation of zirconium cladding alloys. *Acta*
733 *Mater.* **60**, 7132–7149 (2012).
- 734 48. Harlow, W., Lang, A. C., Demaske, B. J., Phillpot, S. R. & Taheri, M. L. Thickness-
735 dependent stabilization of tetragonal ZrO₂ in oxidized zirconium. *Scr. Mater.* **145**, 95–
736 98 (2018).
- 737 49. Baxter, F. *et al.* Phase stability of zirconium oxide films during focused ion beam
738 milling. *J. Nucl. Mater.* **504**, (2018).
- 739 50. Liu, L. New high pressure phases of ZrO₂ and HfO₂. *J. Phys. Chem. Solids* **41**, 331–
740 334 (1980).
- 741 51. Fabris, S., Paxton, A. T. & Finnis, M. W. A stabilization mechanism of zirconia based
742 on oxygen vacancies only. *Acta Mater.* **50**, 5171–5178 (2002).
- 743 52. Smith, D. K. & Newkirk, W. The crystal structure of baddeleyite (monoclinic ZrO₂)
744 and its relation to the polymorphism of ZrO₂. *Acta Crystallogr.* **18**, 983–991 (1965).
- 745 53. Romero, J., Preuss, M. & Quinta Da Fonseca, J. Texture memory and variant selection
746 during phase transformation of a zirconium alloy. *Acta Mater.* **57**, 5501–5511 (2009).
- 747 54. Rauch, E. F. *et al.* Automatic crystal orientation and phase mapping in TEM by
748 precession diffraction. *Microsc. Anal.* **128**, S5–S8 (2008).
- 749 55. Hu, J. *et al.* Identifying suboxide grains at the metal–oxide interface of a corroded Zr–
750 1.0%Nb alloy using (S)TEM, transmission-EBSD and EELS. *Micron* **69**, 35–42
751 (2015).
- 752 56. Liu, J. *et al.* Mechanism of the α -Zr to hexagonal-ZrO transformation and its impact
753 on the corrosion performance of nuclear Zr Alloys. *Prep.* (2019).
- 754 57. Yu, H., Yao, Z., Long, F., Saidi, P. & Daymond, M. R. In situ transmission electron
755 microscopy study of the thermally induced formation of δ' -ZrO in pure Zr and Zr-
756 based alloy. *J. Appl. Crystallogr.* **50**, 1028–1035 (2017).
- 757 58. Luo, Y. & Qin, R. Surface energy and its anisotropy of hexagonal close-packed metals.
758 *Surf. Sci.* **630**, 195–201 (2014).
- 759 59. Bakradze, G., Jeurgens, L. P. H. & Mittemeijer, E. J. The different initial oxidation
760 kinetics of Zr(0001) and Zr(10 0) surfaces The different initial oxidation kinetics of
761 Zr(0001) and Zr(10 10) surfaces. *Cit. J. Appl. Phys.* **110**, 1838 (2011).
- 762 60. Momma, K. & Izumi, F. VESTA 3 for three-dimensional visualization of crystal,
763 volumetric and morphology data. *J. Appl. Crystallogr.* **44**, 1272–1276 (2011).

- 764 61. Ogata, S., Li, J., Hirosaki, N., Shibutani, Y. & Yip, S. Ideal shear strain of metals and
765 ceramics. *Phys. Rev. B* **70**, 104104 (2004).
- 766 62. Lin, J. *et al.* Analysis of zirconium oxide formed during oxidation at 623 K on Zr–
767 2.5Nb and Zircaloy-4. *Mater. Sci. Eng. A* **381**, 104–112 (2004).
- 768 63. Motta, A. T. *et al.* Microstructural Characterization of Oxides Formed on Model Zr
769 Alloys Using Synchrotron Radiation. *J. ASTM Int.* **5**, 101257 (2008).
- 770 64. Spengler, D. J., Motta, A. T., Bajaj, R., Seidensticker, J. R. & Cai, Z. Characterization
771 of Zircaloy-4 corrosion films using microbeam synchrotron radiation. *J. Nucl. Mater.*
772 **464**, 107–118 (2015).
- 773 65. Gabory, B. D., Motta, A. T. & Wang, K. Transmission electron microscopy
774 characterization of Zircaloy-4 and ZIRLO oxide layers. *J. Nucl. Mater.* **456**, 272–280
775 (2015).
- 776 66. Motta, A. *et al.* Microstructure and growth mechanism of oxide layers formed on Zr
777 alloys studied with Micro-Beam synchrotron radiation. *J. ASTM Int.* **2**, 1–26 (2005).
- 778 67. Parise, M., Sicardy, O. & Cailletaud, G. Modelling of the mechanical behavior of the
779 metal–oxide system during Zr alloy oxidation. *J. Nucl. Mater.* **256**, 35–46 (1998).
- 780 68. Gass, M. *et al.* Corrosion of Zircaloys: Relating the microstructural observations to the
781 corrosion kinetics. *J. Nucl. Mater.* **509**, 343–354 (2018).
- 782 69. Mainprice, D., Bachmann, F., Hielscher, R. & Schaeben, H. Descriptive tools for the
783 analysis of texture projects with large datasets using MTEX: Strength, symmetry and
784 components. *Geol. Soc.* **409**, 251–271 (2014).
- 785 70. Garner, A. J. W. Investigating the effect of oxide texture on the corrosion performance
786 of zirconium alloys. (University of Manchester, 2014).

787 **Acknowledgments**

788 **Funding:** Include all funding sources, including grant numbers, complete funding
789 agency names, and recipient’s initials. Each funding source should be listed in a
790 separate paragraph such as:

791 The Engineering and Physical Sciences Research Council UK (EPSRC) through the
792 Centre for Doctoral Training in Advanced Metallic Systems, EP/G036950/1 (MSY,
793 AG, FB, SA)

794 The Engineering and Physical Sciences Research Council UK grand MIDAS
795 EP/S01702X/1 (MP, CPR, PF)

796 University Research Fellowship of the Royal Society (CPR)

797 **Author contributions:**

798 Conceptualization: MSY, AG, FB, SA, CPR, MP, PF

799 Methodology: MSY, AG, FB, SA, CPR, MP, PF

800 Investigation: MSY, AG, FB, SA

801 Visualization: MSY, AG, FB, SA

802 Supervision: CPR, MP, PF

803 Writing—original draft: MSY, AG

804 Writing—review & editing: MSY, AG, SA, CPR, MP, PF

805 **Competing interests:** Authors declare that they have no competing interests.

806 **Data and materials availability:** All data needed to evaluate the conclusions in the paper are
807 included in the paper and/or the Supplementary Materials. Additional data and Jupyter
808 notebooks for exploring the data may be found at [10.5281/zenodo.4737700](https://doi.org/10.5281/zenodo.4737700).
809

Supplementary Files

This is a list of supplementary files associated with this preprint. Click to download.

- [Supplementarymaterial.pdf](#)